MIT Open Access Articles

High Resolution Spectroscopy of X-ray Quasars: Searching for the X-ray Absorption from the Warm-Hot Intergalactic Medium

Massachusetts Institute of Technology

HIGH RESOLUTION SPECTROSCOPY OF X-RAY QUASARS: SEARCHING FOR THE X-RAY ABSORPTION FROM THE WARM-HOT INTERGALACTIC MEDIUM

Taotao Fang[1], Claude R. Canizares[2] and Herman L. Marshall[2]
Draft version February 2, 2008

ABSTRACT

We present a survey of six low to moderate redshift quasars with *Chandra* and *XMM*-Newton. The primary goal is to search for the narrow X-ray absorption lines produced by highly ionized metals in the Warm-Hot Intergalactic Medium. All the X-ray spectra can be fitted by a power law with neutral hydrogen absorption method. The residuals that may caused by additional emission mechanisms or calibration uncertainties are taken account by polynomial in order to search for narrow absorption features. No real absorption line is detected at above 3-σ level in all the spectra. We discuss the implications of the lack of absorption lines for our understanding of the baryon content of the universe and metallicity of the intergalactic medium (IGM). We find that the non-detection of X-ray absorption lines indicates that the metal abundance of the IGM should be smaller than ~ 0.3 solar abundance. We also discuss implications of the non-detection of any local ($z \sim 0$) X-ray absorption associated with the ISM, Galactic halo or local group, such as has been seen along several other lines of sight (LOS). By comparing a pair of LOSs we estimate a lower limit on the hydrogen number density for the ($z \sim 0$) 3C 273 absorber of $n_H \gtrsim 4 \times 10^{-3}\,\mathrm{cm}^{-3}$.

Subject headings: quasars: individual (PG 1407+265, PKS 2135-147, 1H 0414+009, 1ES 1028+511, 3C 279, H 1426+268) — intergalactic medium — quasars: absorption lines — X-rays: galaxies — large-scale structure of universe — methods: data analysis

1. INTRODUCTION

Cosmological hydrodynamic simulations predict that a significant amount of baryons that reside in the Lyα forest at high redshift were subsequently shock-heated to temperatures between 10^5–10^7 K, to form the so-called "Warm-Hot Intergalactic Medium", or WHIM (see, e.g., Hellsten, Gnedin, & Miralda-Escudé 1998; Cen & Ostriker 1999; Davé et al. 2001; Fang, Bryan, & Canizares 2002; Chen, Weinberg, Katz, & Davé 2003; Viel et al. 2003). High temperatures ionized most of the neutral hydrogen, making it impossible to detect the WHIM gas as a low redshift Lyα forest. Thus, one of the central problems in studying the baryonic content of the universe is to detect these "missing baryons".

In principal, such hot intergalactic gas can be probed via both emission and absorption. However, the diffuse nature of the hot gas makes it vary hard to directly image the WHIM gas (see, e.g., Yoshikawa et al. 2003; Fang et al. 2005). On the contrary, much effort has been put into studying the absorption features produced by highly ionized metals in the spectra of background quasars.

In the past few years, significant progress has been made in this field, thanks to the advancement in high resolution spectroscopy provided by the new generation of space telescopes. A significant number of O VI absorption lines have been seen with the Far Ultraviolet Spectroscopic Explorer (*FUSE*) and the Hubble Space Telescope (*HST*) (see, e.g., Savage, Tripp, & Lu 1998; Tripp, Savage, & Jenkins 2000; Tripp & Savage 2000; Simcoe, Sargent, & Rauch 2002). The distribution and derived properties of these O VI lines are consistent with predictions from simulations. In the X-ray band, Fang et al. (2002a), Mathur, Weinberg, & Chen (2002), McKernan et al. (2003), and

Nicastro et al. (2005) reported on the detection of intervening O VII and/or O VIII absorption lines with *Chandra* and *XMM*-Newton. Nicastro et al. (2002), Fang, Sembach, & Canizares (2003), Rasmussen, Kahn, & Paerels (2003), Cagnoni et al. (2004), McKernan et al. (2004), and Williams et al. (2005) also reported the detection of $z \approx 0$ X-ray absorption lines. These low redshift lines may be attributable, at least in part, to the WHIM gas in our Local Group.

Starting from *Chandra* and *XMM*-Newton observation cycle 1, we conducted a survey of X-ray bright quasars to systematically study the potential X-ray absorption lines from the WHIM. In the first round, we observed two high redshift quasars (PKS 2149-306 and S5 0836+710 at $z \sim 2$, see Fang, Marshall, Bryan, & Canizares 2001) and one low redshift quasar (H 1821+643 at $z \sim 0.3$, see Fang et al. 2002b). In this paper, we present the results from our second round of the survey, which includes a total of six *Chandra* and *XMM* targets, and a total exposure time of $\sim$ half-million seconds. These targets were selected largely based on their X-ray flux levels, which were determined by previous X-ray observations such as *ROSAT* and *ASCA*. We also selected these targets because their low Galactic absorption (except 1H 0414+009), and because their relatively simple spectral shape (power law) without any intrinsic features. Two of them were selected because their UV spectra showed O VI absorption lines. In principle, we can either take a deep look at one target, which can probe low column density absorbers, or observe several lines-of-sight to increase the total pathlength. To maximize the potential information we can gain, we selected the second approach.

This paper is organized as follows. We present the tar-

[1] Department of Astronomy, University of California, Berkeley, CA 94530, fangt@astro.berkeley.edu; *Chandra* Fellow

[2] Department of Physics and Center for Space Research, MIT, 77 Mass. Ave., Cambridge, MA 02139
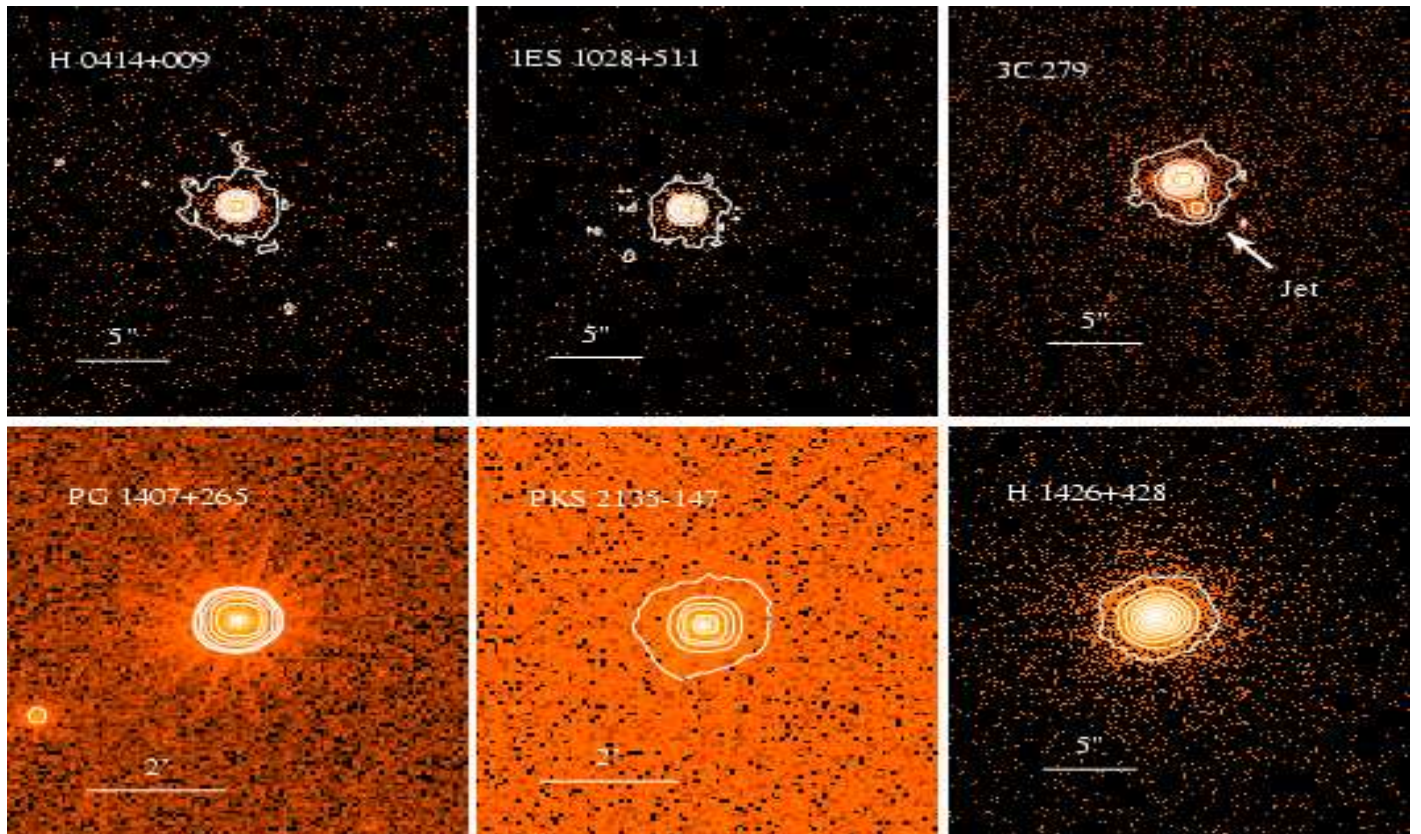
Fig. 1.— X-ray images of all the targets, with north to the top and east to the left. The white line in the bottom of each panel shows the angular size. For the 4 *Chandra* targets, the zeroth order images are shown here; and EPIC images are shown for the two *XMM*-Newton targets.

gets and detailed data reduction procedures in section §2. We show the continuum properties in section §3. In section §4 we discuss how we subtract continuum and do narrow line analysis. Section §5 is devoted to detailed study of the results from narrow line analysis, and section § 6 is summary and discussion.

Table 1: Target Parameters

Target	RA (J2000)	Dec (J2000)	Redshift	N_H $(10^{20} \mathrm{cm}^2)$
PG 1407+265	14 09 23.9	26 18 21	0.940	1.38
PKS 2135-147	21 37 45.2	-14 32 55	0.200	4.77
1H 0414+009	04 16 52.4	01 05 24	0.287	9.15
1ES 1028+511	10 31 18.4	50 53 36	0.361	1.27
3C 279	12 56 11.1	-05 47 22	0.536	2.21
H 1426+428	14 28 32.6	42 40 21	0.129	1.36

2. OBSERVATION AND DATA REDUCTION

Our sample includes six quasars with redshifts ranging from $z \sim 0.13$ to ~ 0.92. Four targets (3C 279, 1ES 1028+511, 1H 0414+009, and H 1426+428) were observed with the High Energy Transmission Grating Spectrometer (HETGS, see Canizares et al. 2005) [3] onboard the *Chandra* X-ray telescope, and two (PG 1407+265 and PKS 2135-147) were observed with the *XMM*-Newton Observatory [4]. We list all the targets in Table 1 and their relevant observational information in Table 2. These targets

[3] See http://space.mit.edu/HETG/.

[4] See http://xmm.vilspa.esa.es/

were selected based on their strong X-ray flux obtained from previous *ROSAT* and/or *ASCA* observations.

Table 2: Observation Log

Target	Telescope	Obs. ID	Obs. Date	Duration (sec)
PG 1407+265	*XMM*	0092850501	2001-12-22	42,062
PKS 2135-147	*XMM*	0092850201	2001-04-29	59,850
1H 0414+009	HETGS	2969	2002-08-01	52,000
		4284	2002-08-02	41,000
1ES 1028+511	HETGS	2970	2002-03-27	25,000
		3472	2002-03-28	75,000
3C 279	HETGS	2971	2002-03-21	107,000
H 1426+428	HETGS	3568	2003-09-08	102,000

2.1. *Chandra Data Analysis*

The *Chandra* HETGS produces a zeroth order image at the aim-point on the focal plane detector, the ACIS-S array, with higher order spectra dispersed to either side (for ACIS-S, see Garmire et al. 2003). For all four *Chandra* observations, the telescope pointing direction was offset $20''$ along +Y in order to move the zeroth order off a detector node boundary, and the Science Instrument Module (SIM) was moved toward the read-out row by about $3\ mm$ to get better ACIS energy resolution (for detailed instrument setups, see the *Chandra* Proposers' Observa-
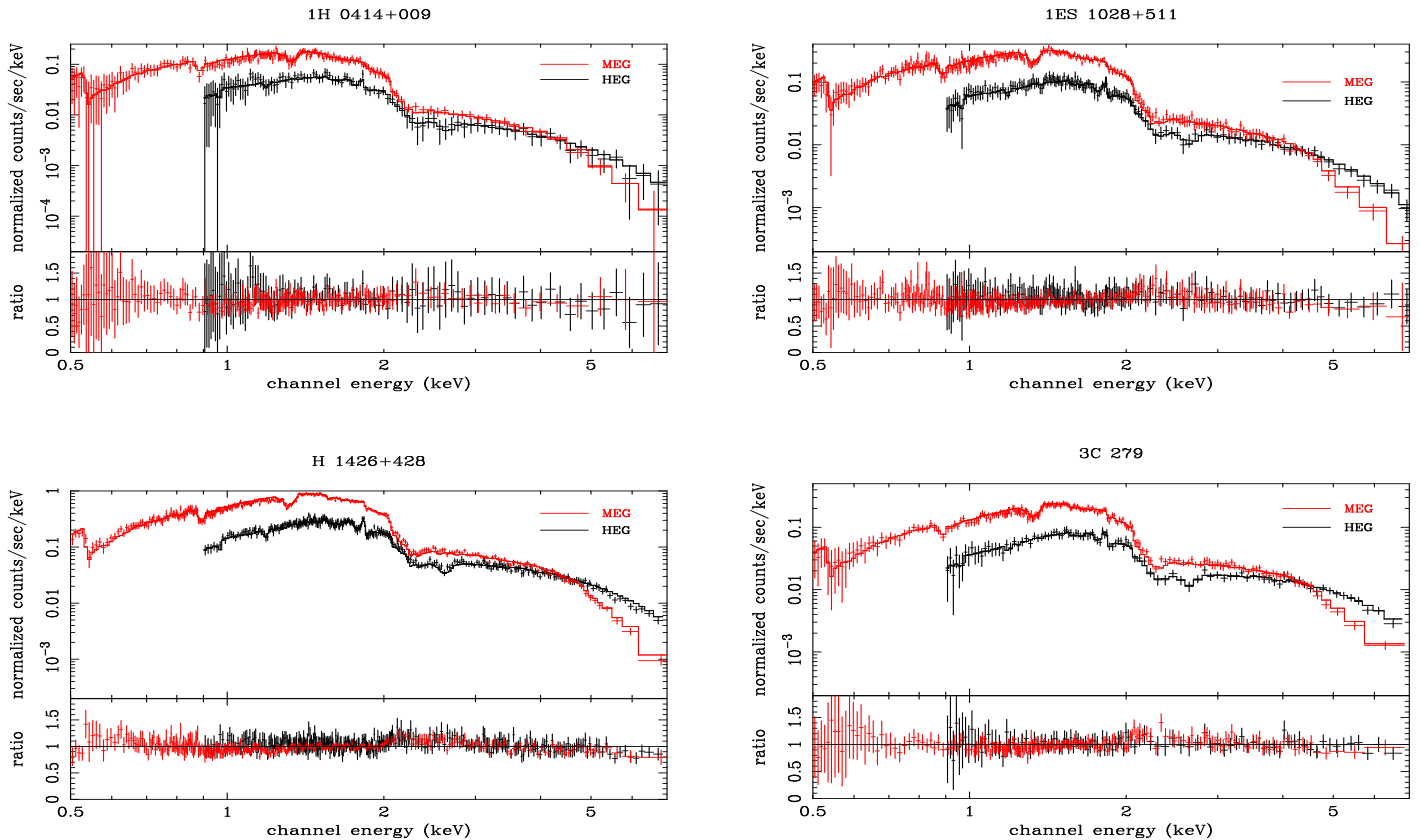
FIG. 2.— *Chandra* MEG (red line) and HEG (dark line) spectra. Solid lines in each plot represent the best fitted models. The bottom panel of each plot shows the ratio between data and model.

tory Guide, or POG[5]). Figure 1a, b, c, and d display the zeroth-order images. We also label a size of 5″ in each panel. 1H 0414+009, 1ES 1028+511, and H 1426+428 appear to be point sources with core sizes less than 2 – 3 ″; however, a large scale jet is clearly presented in the zeroth order image of 3C 279 (south-east direction). Detailed study of this X-ray jet (Marshall, Cheung, Canizares, & Fang 2003) will be presented in a separate paper.

Chandra data were analyzed with the standard pipeline for the *Chandra* HETGS provided by the Chandra X-ray Center (CXC)[6]. We use *Chandra* Interactive Analysis of Observations (CIAO) V3.0. The standard screening criteria were applied to the data. We select photon events with *ASCA* grades 0, 2, 3, 4, 6 and excluded those with energies above 10 keV. We also remove hot columns and bad pixels in each CCD chip. and take into account the effect of ACIS absorption. The HETGS consists of two different grating assemblies, the High Energy Grating (HEG) and the Medium Energy Grating (MEG), and provides nearly constant spectral resolution ($\Delta\lambda = 0.012\mathring{A}$ for HEG and $\Delta\lambda = 0.023\mathring{A}$ for MEG) through the entire bandpass (HEG: 0.8-10 keV, MEG: 0.4-8 keV). The moderate energy resolution of the CCD detector ACIS-S is used to separate the overlapping orders of the dispersed spectrum. We added the plus and minus sides to obtain the first order spectra of both grating assemblies. In cases where two observations were performed for one

target (1H 0414+009 and 1ES 1028+511), we use CIAO tool "add_grating_spectra" to add two spectra together, and average the auxiliary response files (ARF).

2.2. *XMM-Newton Data Analysis*

We obtained data for PG 1407+265 and PKS 2135-147 with all the instruments onboard *XMM*-Newton, and here we focus on EPIC (including MOS1, MOS2 and PN) and RGS (including RGS1 and RGS2) data. While with high spectral resolution RGS data will be analyzed to study narrow line features, we also study EPIC data to obtain information regarding the QSO continuum. Figure 1e and f shows the MOS images of both QSOs.

All the EPIC observations were performed with the "PrimeFullWindow" and "Imaging" data mode. A medium filter was applied. Data were processed with the standard software, *XMM*-Newton Science Analysis System (SAS) V5.4 [7]. We applied the standard SAS tasks "emchain" and "epchain" to obtain event files for MOS and PN data, respectively. We selected events with patterns between 0 and 12 for MOS and those with patterns between 0 and 4 for PN. All events within central region with a radius of 30″ were extracted for the point source spectra and areas between 30″ and 60″ for the background spectra. We also checked the pile-up level with the SAS task "epatploy" and found that there is no significant pile-up between 0.4 and 10 keV, so we chose this energy

---

[5] See *Chandra* Proposers' Observatory Guild (POG) at http://asc.harvard.edu.

[6] See http://asc.harvard.edu/

[7] see http://xmm.vilspa.esa.es/
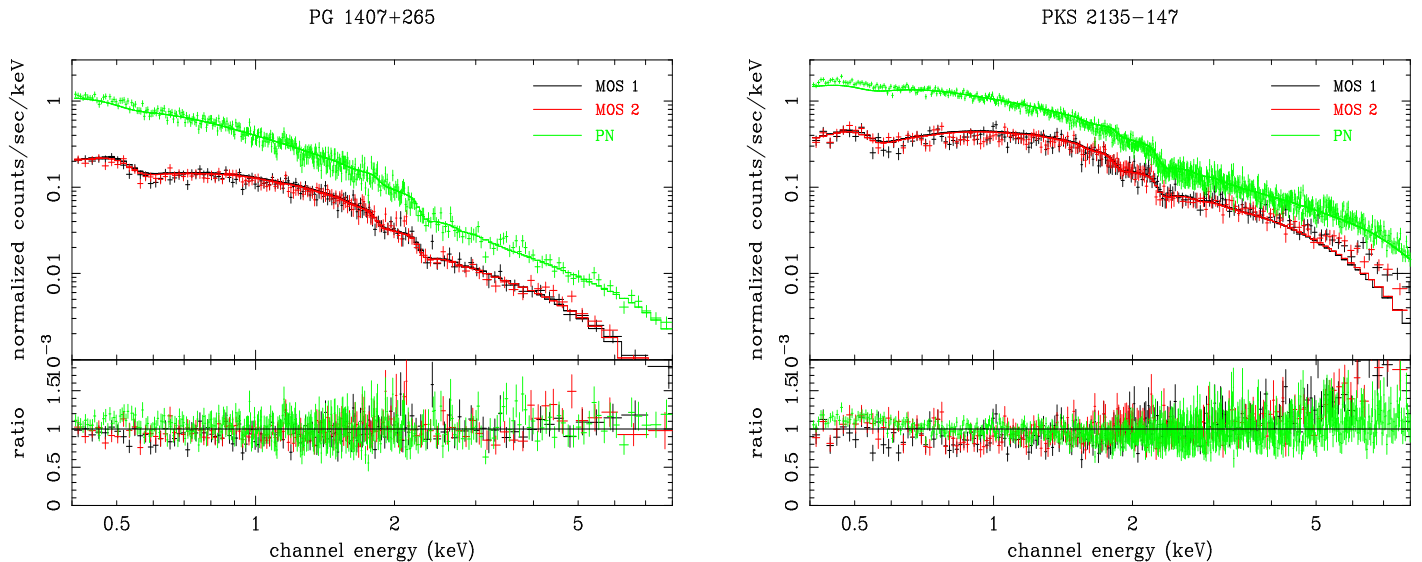
PG 1407+265

PKS 2135−147

FIG. 3.— *XMM*-Newton MOS1 (dark), MOS2 (red), and PN (green) spectra. Solid lines in each plot represent the best fitted models. The bottom panel of each plot shows the ratio between data and model.

range for the subsequent spectral fitting. Finally, all the spectra were binned to have a minimum of 20 counts per bin.

RGS 1 and 2 spectra were extracted using "`rgsproc`". This SAS task also provided a combined RMF and ARF file for each spectrum. To achieve the highest signal-to-noise, we added both RGS (including the first and second order spectra) together. The combined spectrum was then grouped channel by channel to have a constant bin size of $0.025 \, \AA$, half of the width of the RGS FWHM, for the subsequent narrow line analysis.

3. CONTINUUM PROPERTIES OF INDIVIDUAL SOURCE

Continuum can be fitted by a power law with absorption from neutral hydrogen. The flux $F(E)$ can be expressed as

$$F(E) = A_{pl} \left(\frac{E}{1 \, \mathrm{keV}} \right)^{-\Gamma} \exp\left[-\sigma(E) N_H\right]. \qquad (1)$$

Here A_{pl} is the normalization at 1 keV, Γ is the photon index, E is the photon energy, $\sigma(E)$ is the photoionization cross section, and N_H is the neutral hydrogen column density. Table 3 lists the fitting parameters for all the targets and inferred fluxes and luminosities. Fitting was performed with XSPEC V11.3 [8]. For each *Chandra* data set we fit with with two models: (a) a power law with a fixed neutral hydrogen absorption at the Galactic level, and (b) a power law with a variable hydrogen absorption, and we fit both HEG and MEG data simultaneously (see Figure 2). The fitting is performed between 0.9 and 8 KeV HEG, and 0.5 and 8 keV for MEG. In the top four targets in Table 3, the first rows show the fitted results from model (a) and the second rows show results from model (b). For the two *XMM* targets, since we cannot constrain the hydrogen column density (N_H), we fix them at the Galactic value and fit the data with model (a) only. The fitting performed with all the three instruments (MOS1, MOS2 and PN) simultaneously (see Figure 3), between 0.4 and 10 Kev. We emphasize that

while from the power law fit some spectra show residuals that suggest additional emission mechanisms, we are not trying to understand the emission processes but only need to fit continuum to search for absorption lines. In the next section, these residuals will be taken into account by polynomials in order to search for narrow features. Since in many places of the spectra we have to deal with small number of photons per bin, we fit the spectrum using *C*-statistics in stead of the conventional χ^2-statistics (Cash 1976). In Table 3 and following sections, errors are quoted as 90% confidence unless otherwise mentioned.

Comments on individual sources:

- *3C 279*: This source is a radio loud quasar (RLQ) and was identified as the first superluminal source (Whitney et al. 1971). Our *Chandra* observation, for the first time, revealed the jet in X-ray band (for detail see Marshall, Cheung, Canizares, & Fang 2003). While both *ROSAT* (Comastri, Fossati, Ghisellini, & Molendi 1997; Sambruna 1997) and *ASCA* (Reeves & Turner 2000) observations showed similar photon indices ($\Gamma \sim 1.8$), we obtained a relatively flat spectrum with *Chandra* ($\Gamma \sim 1.5 - 1.6$). The fluxes and luminosities are consistent among these observations.

- *H 1426+428*: This is a BL Lac object and was extensively observed with *HEAO-1* (Wood et al. 1984), *EXOSAT* (Remillard et al. 1989), *BBXRT* (Madejski et al. 1992), *ROSAT* and *ASCA* (see,e.g.,Sambruna et al. 1997), and *BeppoSAX* (Costamante et al. 2001). Our result shows that the fitted N_H is significantly higher than the Galactic value, which is consistent with results from *BBXRT* and *ASCA* but not with *ROSAT* (Sambruna et al. 1997). The observed flux between 2 — 10 keV varied from ~ 2 to $\sim 5 \times 10^{-11} \, \mathrm{ergs \, cm^{-2} s^{-1}}$ among various observations, while the photon index varies

[8] see http://heasarc.gsfc.nasa.gov/docs/xanadu/xspec/

Table 3: Spectral Fitting Parameters

Target	N_H $(10^{20}\,\mathrm{cm}^2)$	Photon Index (Γ)	$A_{pl}{}^a$	$f_{2-10}{}^b$	$L_{2-10}{}^c$	$C - stat/\mathrm{dof}$
3C 279	2.21^d	1.52 ± 0.01	3.00 ± 0.03	1.4	1.5×10^{46}	1125/950
	5.0 ± 1.0	1.57 ± 0.02	3.19 ± 0.07	1.3	1.5×10^{46}	1104/949
H 1426+428	1.36^d	1.80 ± 0.01	11.87 ± 0.07	3.6	1.7×10^{45}	2098/950
	9.7 ± 0.5	1.98 ± 0.02	14.35 ± 0.20	3.4	1.6×10^{45}	1456/949
1H 0414+009	9.15^d	2.49 ± 0.02	3.34 ± 0.05	0.4	1.2×10^{45}	1079/950
	$11.88^{+1.84}_{-1.32}$	2.57 ± 0.04	3.57 ± 0.13	0.4	1.2×10^{45}	1068/949
1ES 1028+511	1.27^d	2.11 ± 0.02	4.83 ± 0.05	0.9	4.8×10^{45}	1153/950
	$5.98^{+0.70}_{-0.90}$	2.24 ± 0.02	5.43 ± 0.13	0.9	4.7×10^{45}	1075/949
PG 1407+265	1.38^d	$2.24^{+0.01}_{-0.02}$	0.44 ± 0.01	0.08	4.2×10^{45}	956/986
PKS 2135-147	4.77^d	1.81 ± 0.01	1.65 ± 0.01	0.6	6.2×10^{44}	2400/1521

a. Flux at 1 keV (observer's frame) in units of $10^{-3}\,\mathrm{photons\,cm^{-1}s^{-1}keV^{-1}}$.
b. Flux between $2 - 10$ keV (observer's frame), in units of $10^{-11}\,\mathrm{ergs\,cm^{-2}s^{-1}}$.
c. Intrinsic luminosity between $2 - 10$ keV, in units of $\mathrm{ergs\,s^{-1}}$.
d. N_H fixed at the Galactic values.

slightly around 2. While *BBXRT* reported an X-ray absorption feature at ~ 0.66 keV (Madejski et al. 1992; Sambruna et al. 1997), we could not confirm this in our *Chandra* MEG spectrum, consistent with results from recent *XMM*-Newton observations (Blustin, Page, & Branduardi-Raymont 2004).

- *H 0414+009*: This target is a BL Lac object associated with a galaxy cluster of Abell richness of 0 (Falomo, Pesce, & Treves 1993). *BeppoSAX* and *ROSAT* observations (Wolter et al. 1998) showed similar photon indices. However, we obtain a lower $2 - 10$ keV flux, indicating flux variation by a factor of ~ 2. We also find a slightly high N_H, compared with the Galactic value.

- *1ES 1028+511*: The redshift of this BL Lac object has been accurately determined as $z = 0.361$, based on the measurement of two Ca II absorption lines (Polomski et al. 1997). *ROSAT* observation showed a power law spectrum with $\Gamma = 2.43 \pm 0.20$ and an unabsorbed flux of $6.16 \times 10^{-11}\,\mathrm{ergs\,cm^{-2}s^{-1}}$ between $0.5 - 2.4$ keV. This source was also among sources that listed in the *ASCA* Medium Sensitive Survey (Ueda et al. 2001) with a flux of $7.77 \times 10^{-12}\,\mathrm{ergs\,cm^{-2}s^{-1}}$ between $2 - 10$ keV, assuming a photon index of 1.7.

- *PG 1407+265* It's one of the brightest quasars at redshift around 1. There is weak evidence for Damped Lyα Absorption and for Lyman Limit System in its optical continuum (Lanzetta, Wolfe, & Turnshek 1995). A *HST* observation revealed intrinsic narrow absorption features of O VI and Lyα in the quasar rest frame (Ganguly et al. 2001). Previous *ASCA* observation showed a spectrum with similar photon index ($\Gamma \sim 2$) but stronger $2 - 10$ keV flux (Reeves & Turner 2000).

- *PKS 2135-147*: This is a typical double-lobe, radio source (Miley & Hartsuijker 1978; Gower & Hutchings 1984). X-ray observations with *Einstein* (Wilkes & Elvis 1987) and *EXOSAT* (Singh, Rao, & Vahia 1991) reported a photon index consistent with our observation; however, *ROSAT* observations (Rachen, Mannheim, & Biermann 1996) showed a much steeper spectrum, with $\Gamma \sim 2.5$. We also obtained a lower X-ray flux, compared with previous observations. Optical and UV spectra show strong absorption lines of O VI, N V and Lyα at $z_{abs} \sim z_{em}$ (Hamann et al. 1997). These absorption lines also lie near the center of a small cluster and is very close to three galaxies inside that cluster. It is still unclear whether these absorption lines are intrinsic or due to the intervening systems.

4. NARROW LINE ANALYSIS

Cosmological simulations predict that typical X-ray absorption lines from the WHIM gas have line widths on the order of mÅ due to velocity broadening (see, e.g., Hellsten, Gnedin, & Miralda-Escudé 1998; Fang, Bryan, & Canizares 2002; Chen, Weinberg, Katz, & Davé 2003). On the observation side, the detection of such narrow features relies on a careful measurement of the continuum level. Using 1ES 1028+511 as an example, in Figure 4 we show how we obtain a continuum-subtracted spectrum.

Figure 4 shows a small portion of the raw count spectrum of 1ES 1028+511 plotted against wavelength. The solid dark line in the top panel shows the MEG first order counts between 5 and 7 Å, with a bin size of 0.02Å. The bin size is chosen in such a way that there are *at least* two bins across the FWHM of the point spread function (PSF) of the instrument. In this way the bin size is 0.005Å for *Chandra* HEG, 0.01Å for MEG and 0.025Å for *XMM* RGS [9]. The red line (labeled model 1) shows the contin-

[9] See   http://asc.harvard.edu/proposer/POG/html/HETG.html   and
http://xmm.vilspa.esa.es/external/xmm_user_support/documentation/uhb/node45.html for the width of instrument PSF of *Chandra* HETG and *XMM* RGS, respectively.

uum from a power law plus neutral hydrogen absorption, with the fitting parameters adopted from Table 2.2. The bottom panel gives χ, which effectively is the corresponding Gaussian sigma of the Poisson distribution (Gehrels 1986).

While on scales larger than ~ 1 Å the absorbed power law provides a good fit to the overall spectrum, in some local regions it will either over or under-estimate the observed counts due to instrumental or intrinsic fluctuations. Clearly, in the bottom panel of Figure 4, there are more red bins above zero than bins below zero, which means in the 5 – 7Å region, model 1 underestimates the observed counts. The discrepancy amounts to $\sim 10\%$. Using such a model could compromise the search for narrow absorption or emission lines. To eliminate this problem, we first obtain the residual spectra by subtracting model 1. We then divide the whole residual spectra into several small regions, and in each region we fit the residual with a 3-order polynomial. To avoid significant deviation caused by one or two randomly high or low χ bins, we ignore all the bins with $|\chi| > 3$ before fitting. The selected spectral ranges are 2 and 30 Å for MEG, 2 and 14 Å for HEG, and 5 and 35 Å for RGS. The region size is 4 Å, 4 Å, and 5 Å, for MEG, HEG, and RGS, respectively. This method allows us to minimize the fluctuations at large scales, and still preserve features with width narrower than 1 to 2 Å, which approximately is the region size divided by the order of the fitted polynomial. We find the histogram distribution of the χ obtained in this method can be well fitted by a Gaussian distribution. We call this method "model 2" and plot it in blue in Figure 4. Clearly, model 2 provides a significantly better fit to the observed continuum. From Figure 5 to 10 we showed the data and the best fitted results from "model 2".
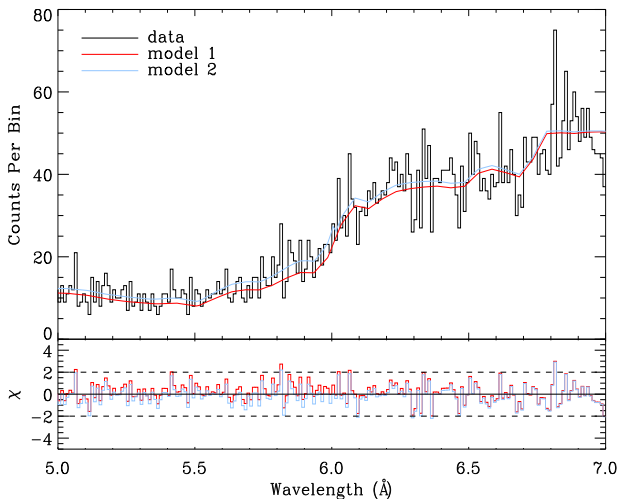

FIG. 4.— A sample of data (dark) and comparison between two models. Model 1 (shown in red) adopted simplily the best fitted model from Table 2.2, and model 2 (blue) uses an local fitting technique. Bottom panel shows the χ, the equivalent Gaussian σ of Poisson distribution of each model. Clearly, model 2 is a better fit to data.

The next step is to identify any potential absorption (or emission) features in the spectrum. Our search criterion is still based on χ: we search for any feature which has

[10] see http://space.mit.edu/ASC/ISIS/

at least two continuous bins with $|\chi| > \chi_{min}$. Assuming the signal-to-noise ratio (SNR) in the first bin is χ_1 and in the next bin is χ_2, Total SNR in these two bins follows $\chi = (\chi_1 + \chi_2)/\sqrt{2}$. To ensure a minimum detection of at least 3σ, we need to have both χ_1 and $\chi_2 \lesssim -2$ for absorption features and both χ_1 and $\chi_2 \gtrsim 2$ for absorption features. We label features identified with this requirement as potential absorption or emission lines. We then fit the continuum-subtracted residual with a Gaussian line profile around the features we identified. The subtraction and fitting are performed with the software package ISIS (Interactive Spectral Interpretation System, see Houck & Denicola 2000) [10]

Combining all the data together, we have a total of $\sim$ 20,000 bins. Based on the above criteria, we find a total of 28 possible absorption features. Other stringent criteria are enforced to eliminate false detections, including that (1) a true feature should appear in both MEG and HEG spectra for *Chandra* targets; (2) if a feature appears in MEG only (at wavelength longer than 14 Å), it should appear in both +1 and −1 orders; (3) for RGS, a true detection should appear in both RGS-1 and RGS-2; and (4) we should avoid regions right at the instrument features - these regions typically show large discrepancies between model and data. With these criteria no real feature is detected. We also searched for emission features and find no significant detections.

Other methods have been applied to fit the continuum and detect narrow absorption features. For example, McKernan et al. (2004) added an inverted Gaussian to a physically-motivated continuum model and searched for absorption features by monitoring changes in fit statistics. To compare these two methods, we make a faked spectrum by adding narrow features to an absorbed power law continuum and then apply both methods. We find that both methods can effectively identify narrow absorption lines with nearly the same significance. However, our method is more robust when the underlying continuum is more complex and has unknown components, and when there are uncertainties in continuum calibration.

5. DISCUSSION

5.1. *Intervening IGM Absorption*

Based on the non-detection of any significant absorption features, we can determine the minimum detectable ion column densities at a certain SNR level. Given the quasar continuum flux f_X, the minimum detectable line equivalent width (W_λ) is

$$W_\lambda = SNR \times \left(\frac{\lambda}{f_X RAT} \right)^{\frac{1}{2}}, \qquad (2)$$

where λ is wavelength, $R \equiv \lambda/\Delta\lambda$ is the resolving power, A is the effective area and T is the exposure time. We expect weak, unresolved features from the linear part of the curve-of-growth. The minimum detectable column density (N_i) and equivalent width W_λ then follow the linear relationship (Spitzer 1978)

$$\frac{W_\lambda}{\lambda} = 8.51 \times 10^{-13} N_i \lambda f. \qquad (3)$$

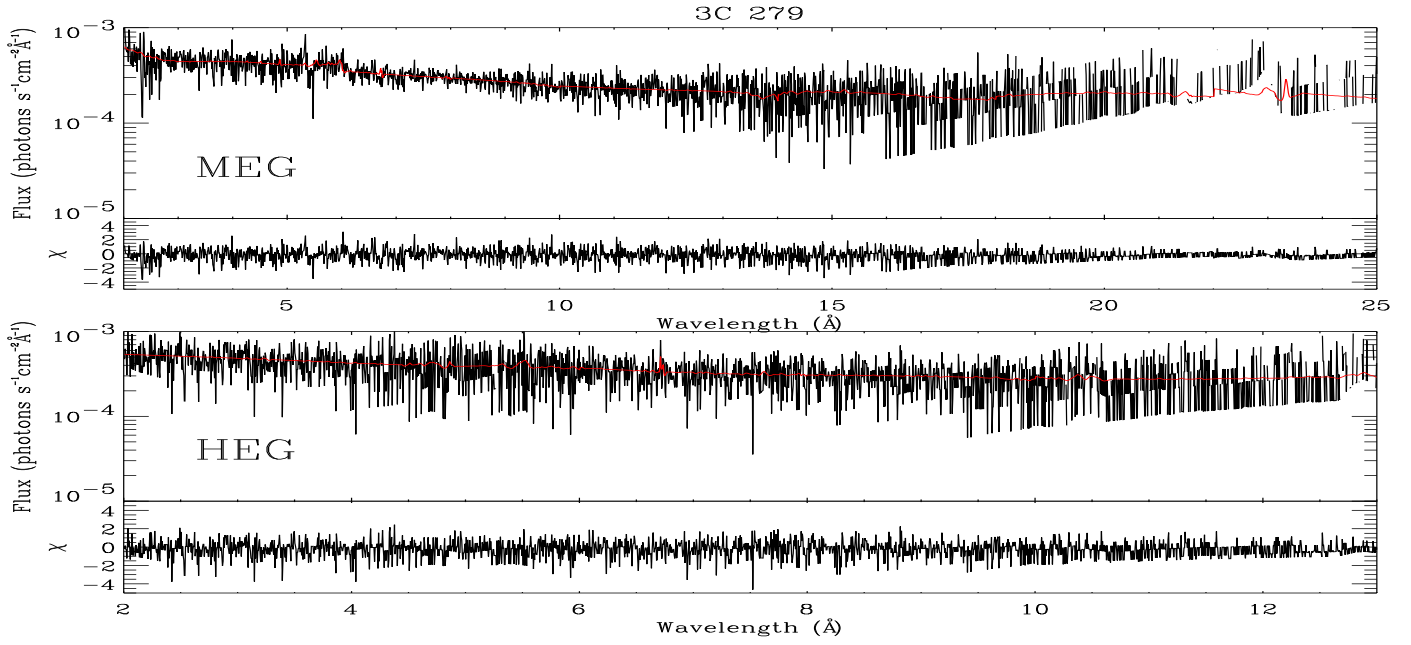Here f is the oscillator strength.

FIG. 5.— *Chandra* MEG (top panel) and HEG (bottom panel) spectra of 3C 279. Red lines show best fitted spectra from model 2. The bottom of each panel show the χ.
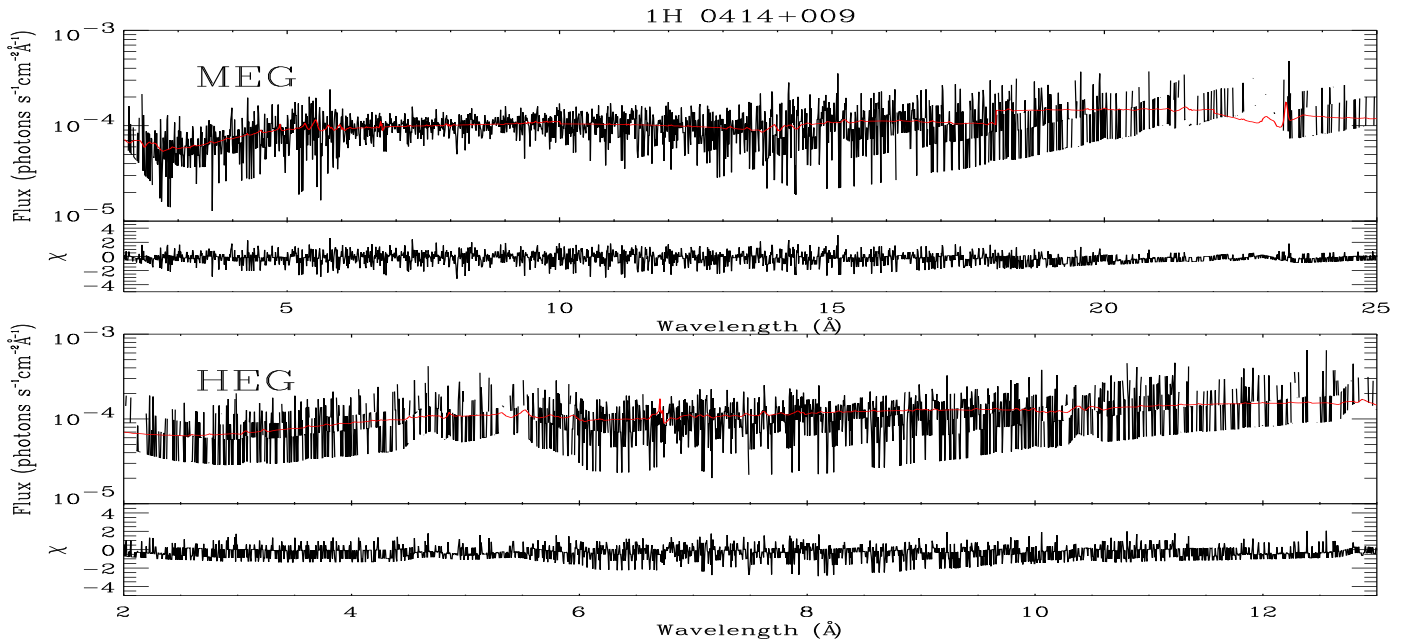

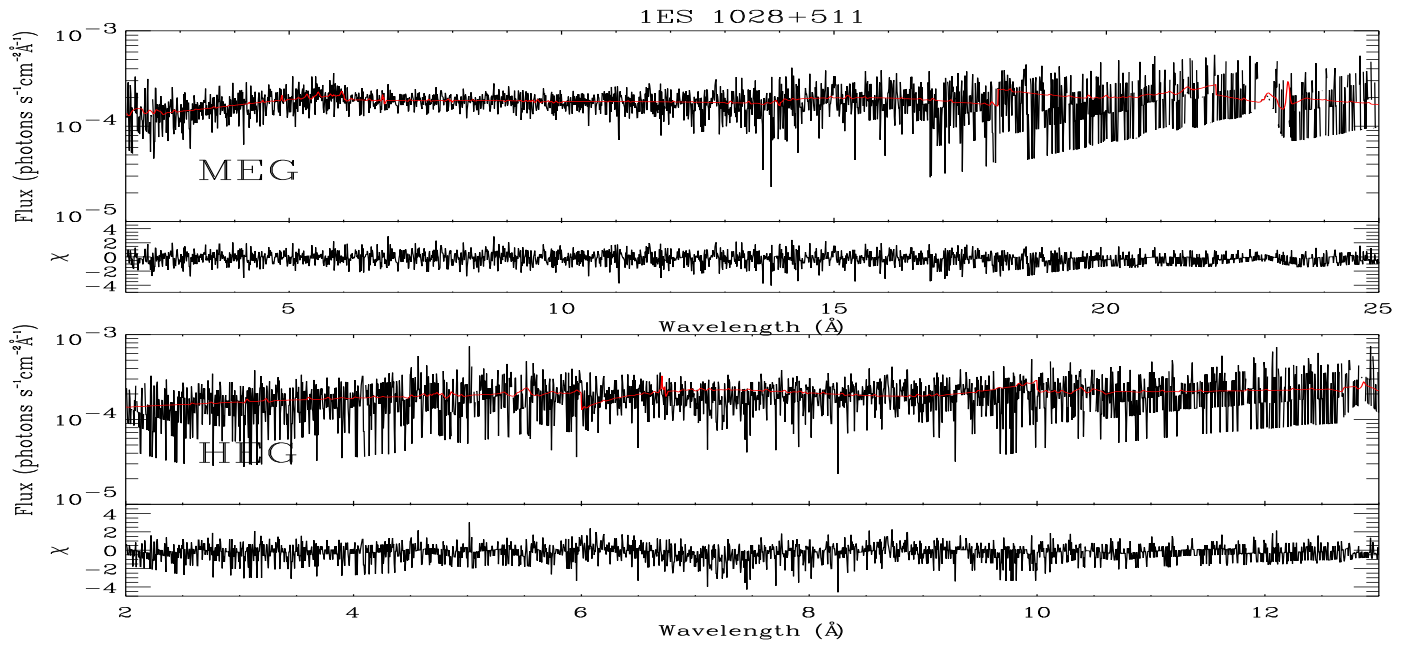FIG. 6.— Same as Figure 5 but for 1H 0414+009.

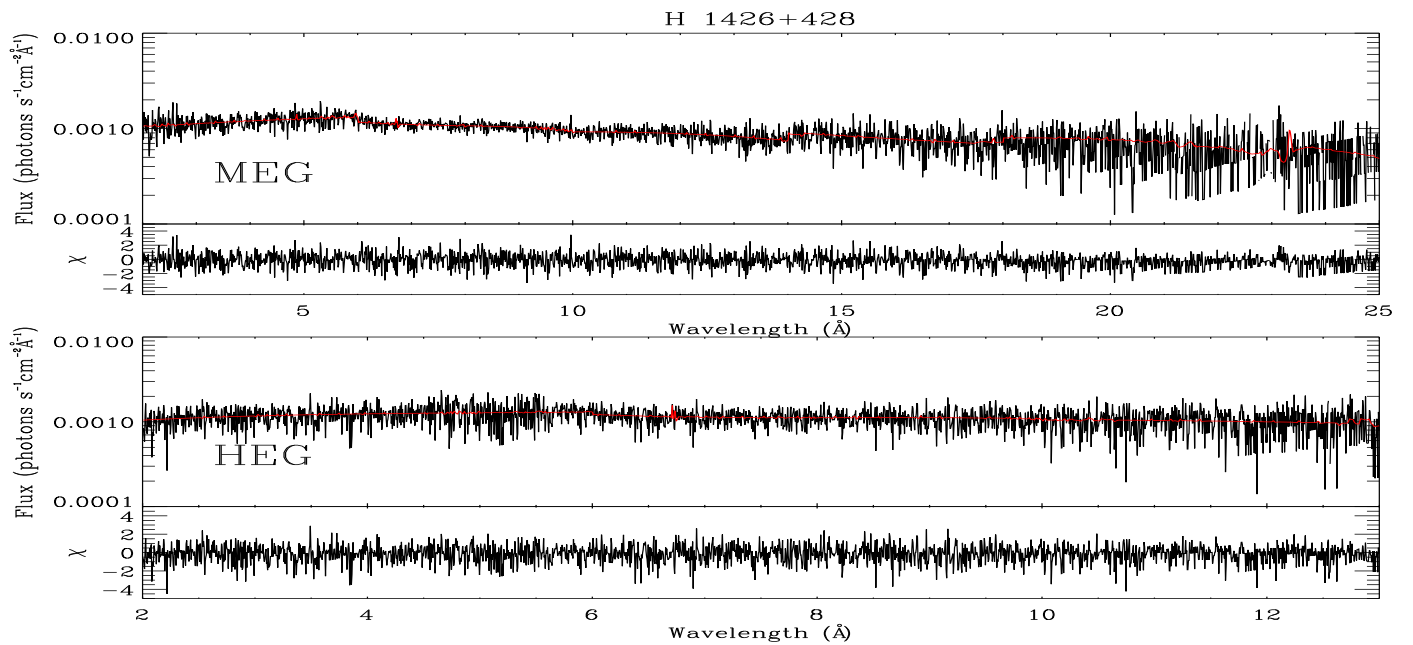FIG. 7.— Same as Figure 5 but for 1ES 1028+511.
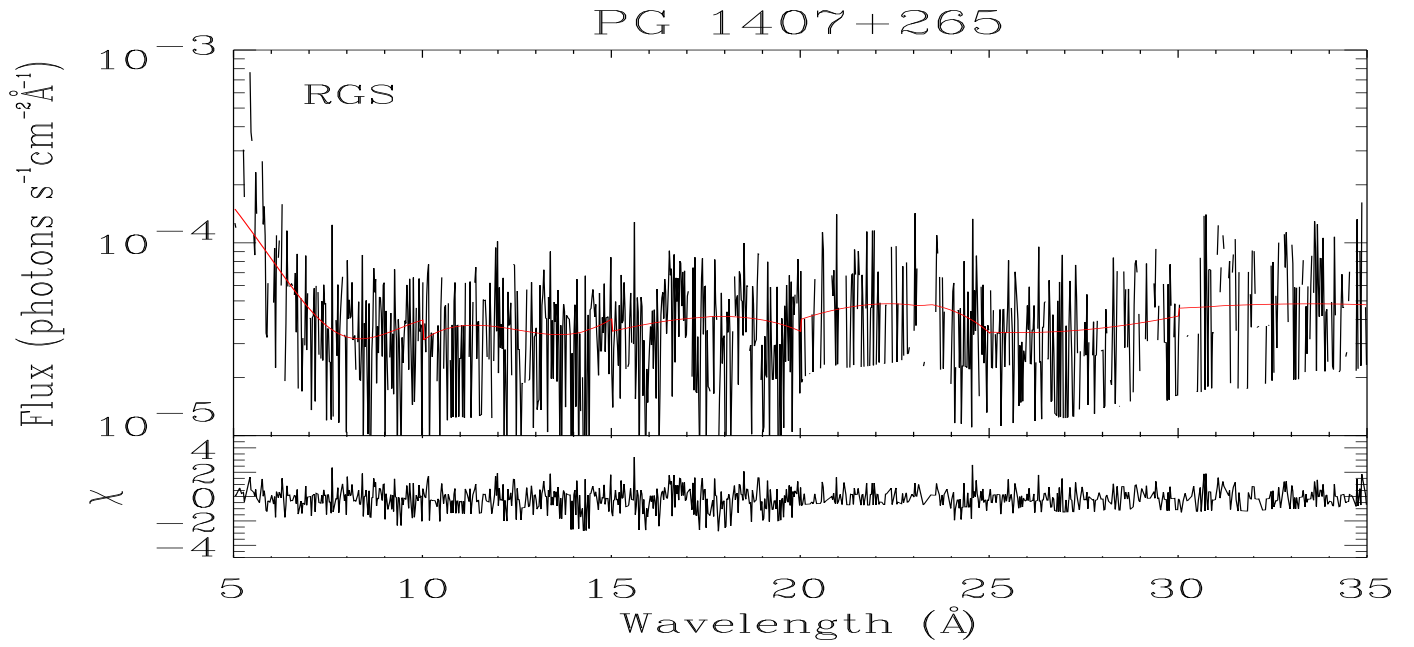

FIG. 8.— Same as Figure 5 but for H 1426+428.

FIG. 9.— *XMM*-Newton RGS spectrum of PG 1407+265. Lines are the same as those in Figure 5.
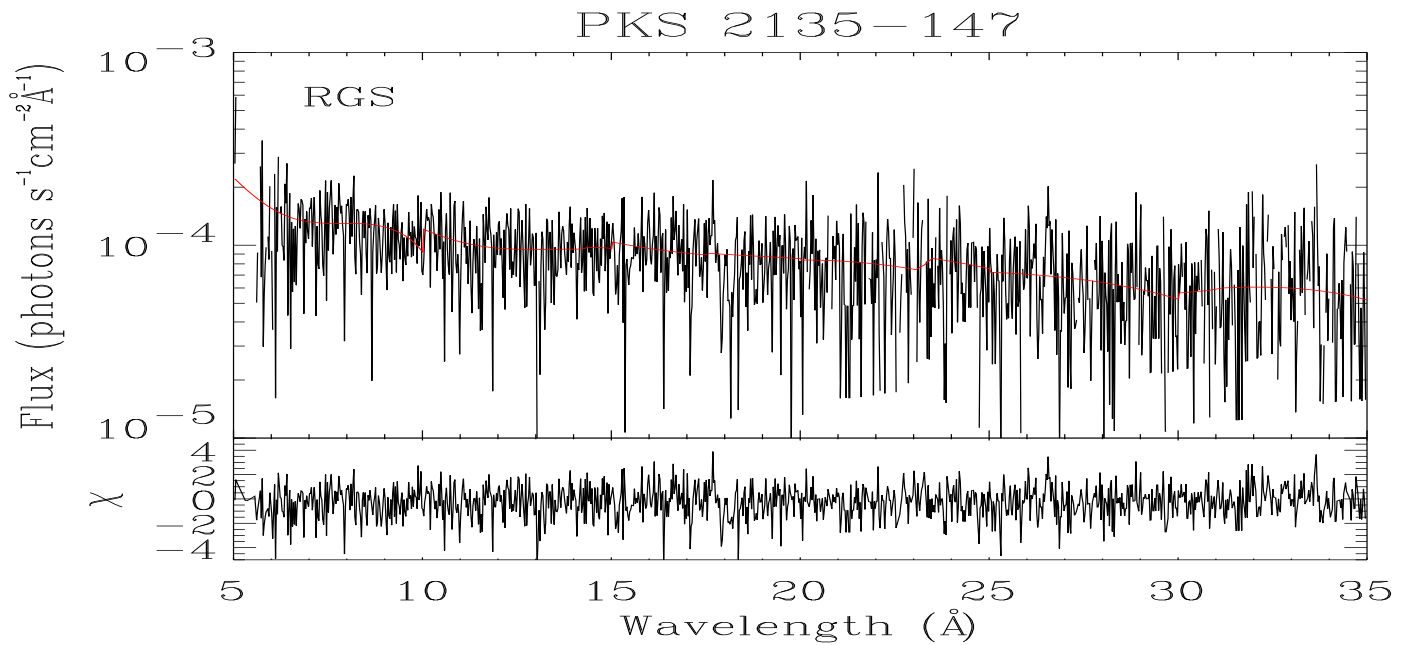

FIG. 10.— *XMM*-Newton RGS spectrum of PKS 2135-147. Lines are the same as those in Figure 5.

In Table 4 we list the minimum detectable column densities of O VII and O VIII along the line-of-sight towards these six targets. We adopt a SNR of 3 here. The rest frame wavelengths of O VII and O VIII are 21.6019 Å and 18.9689 Å, respectively (Verner, Verner, & Ferland 1996). Since *Chandra* HEG has no effective area in the longer wavelength of both transitions, we use MEG only for the four *Chandra* targets. Since MEG has no effective area above 25 – 26 Å, we can probe the line detection up to $z \sim min(z_i, 0.35)$ for O VIII and $z \sim min(z_i, 0.2)$ for O VII, where z_i is the redshift of individual sources.

Table 4: 3σ Limits on Column Density[a]

Target	O VIII	O VII
1H 0414+009	1.87	1.12
1ES 1028+511	1.44	0.86
H 1426+428	1.00	0.60
3C 279	1.87	1.12
PG 1407+265	2.29	1.37
PKS 2135-147	2.36	1.02

a. All column densities are in units of $10^{16} \, \mathrm{cm^{-2}}$.

Using standard cosmological models and ingredients from galaxy and large scale structure evolution, numerical simulations predict the spatial distribution of metals and their ionization structures (see, e.g., Cen & Ostriker 1999). Such simulations allow us to make quantitative predictions of the absorption features that could be present in the spectra of background sources (see, e.g., Hellsten, Gnedin, & Miralda-Escudé 1998; Fang, Bryan, & Canizares 2002; Chen, Weinberg, Katz, & Davé 2003). Our non-detection of any significant absorption lines can, conveniently, put constraints on cosmological parameters and other physical processes adopted in the simulations.

Rather than running complicated hydrodynamic simulations with various cosmological parameters and physical processes to explore the parameter space that can be constrained by our observation results, we adopted a simple but effective analytic approach that follows Perna & Loeb (1998) and Fang & Canizares (2000). The basic idea is that all the hot gas is distributed within virialized halos that follow a Press-Schechter distribution (Press & Schechter 1974). Given a certain density profile of a virialized halo, the probability that a random line-of-sight that passes through a halo of mass M with an impact parameter b can be calculated. Based on assumptions of metal abundance, we can then calculate the so-called "X-ray Forest Distribution Function" (XFDF), defined as $\partial^2 P/(\partial N_i \partial z)$, the absorption line number per unit redshift (z) per column density (N_i) for ion species i. Specifically, XFDF can be analytically calculated as

$$\frac{\partial^2 P}{\partial N_i \partial z} = \int_M \frac{dn}{dM} \frac{d\Sigma}{dN_i} \frac{dl}{dz}, \qquad (4)$$

where (dn/dM) is the distribution of the comoving virialized halo, Σ is the cross section of the halo, and l is the path length.

How accurate is this analytic approach? Fang, Bryan, & Canizares (2002) compared both numerical and semi-analytic methods (with the above analytic model and a halo temperature profile fitted from simulations). For O VII and O VIII, it turns out that there is a large discrepancy in the low column density region ($N_i \sim 10^{12} -$

$10^{15} \, \mathrm{cm^{-2}}$), where most lines are distributed in the filamentary structures seen in the numerical simulations but which cannot be described by Press-Schechter formalism. At the high column density end ($N_i \gtrsim 10^{15} \, \mathrm{cm^{-2}}$), the semi-analytic method provides a reasonablely good fit to results from numerical simulations. These high column density lines distribute typically in virialized halos with higher temperatures and densities than found in the filaments. Since in our study the minimum detectable column densities are around $10^{16} \, \mathrm{cm^{-2}}$, the analytic estimate is appropriate.

Given the XFDF and certain cosmological parameters, we can calculate the expected absorption line number by combining observations on all the six targets. The total absorption line number is then

$$n = \sum_j \int_{N_i(j)}^{\infty} \int_0^{z_j} \frac{\partial^2 P}{\partial N_i \partial z} dN_i dz. \qquad (5)$$

Here $N_i(j)$ is the minimum detectable column density of ion i for the jth target; z_j is its maximum redshift that can be probed with the *Chandra* and *XMM*-Newton instruments; and overall summation is over all the six targets (index j).

The parameters we plan to constrain are the cosmic matter density Ω_m and metal abundance Z (in units of the solar abundance $Z_\odot$.) Changes in these two parameters will dramatically change gas and metal content and could have significantly impact on the detectability of X-ray absorption lines. We keep all the other parameters at the standard values: we use the ΛCDM model with a dark energy density of $\Omega_\Lambda = 1 - \Omega_m$, the Hubble constant is $H_0 = 100h \, \mathrm{km \, s^{-1} Mpc^{-1}}$ with $h = 0.67$; the baryon density is $\Omega_b = 0.04$; and we assume the gas fraction, or the ratio of baryonic-to-total mass, is $f_{gas} = 0.2$.
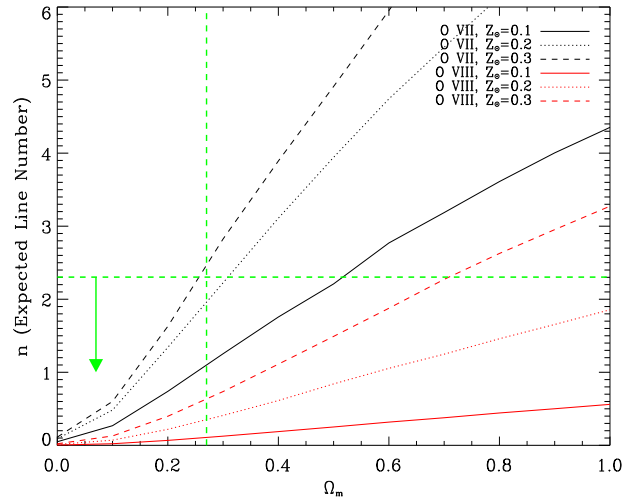

FIG. 11.— the expected total O VII (dark lines) and O VIII (red lines) line numbers with different Ω_m and metal abundance Z. The horizontal green line shows the 90 % confidence upper limit from the non detection of absorption line in our sample. The vertical green line shows the value of Ω_m measured with *WMAP* (Spergel et al. 2003). The green arrow indicates allowed region.

Figure 11 shows the expected total O VII (black lines) and O VIII (red lines) line numbers with different Ω_m and metal abundance Z. Since we detect no absorption line, the horizontal green line shows the 90% confidence upper limit (Gehrels 1986). The vertical green line shows the

value of Ω_m measured with *WMAP* (Spergel et al. 2003). The green arrow indicates allowed region. Clearly, we expect to observe more absorption lines with higher values of metallicity and Ω_m. The degeneracy between metallicity and Ω_m can be broken by applying the much more accurate value of Ω_m measured with *WMAP* (Spergel et al. 2003): $\Omega_m h^2 = 0.14$, indicated by the vertical green line in Figure 11. We cannot constrain metallicity of the IGM based on the measurement of O VIII, i.e., the predicted line number is still less than the 90% upper limit from our observation even if the metallicity is as high as $0.3 Z_\odot$. However, O VII can put much better constraint on the IGM metallicity: for a *WMAP* value of Ω_m, the metal abundance should be smaller than $\sim 0.3 Z_\odot$. That O VII is more restrictive is not surprising: in the collisionally ionized WHIM gas, simulations showed that O VII is more abundant than O VIII and should produce more absorption lines (see Figure 13 of Fang, Bryan, & Canizares 2002).

5.2. *Local ($z \approx 0$) Absorption*

Recently, there are a number of observations of quasars showing local ($z \approx 0$) X-ray absorption lines along several line-of-sight. These background quasars (see, Kaspi et al. 2002; Nicastro et al. 2002; Fang, Sembach, & Canizares 2003; Rasmussen, Kahn, & Paerels 2003; Cagnoni et al. 2004; McKernan et al. 2004) are among the brightest extragalactic X-ray sources in the sky (some of them are used as instrument calibration targets). In particular, McKernan et al. (2004) conducted a survey of nearby type I AGNs, and found that about half of their sample exhibit local ($z \approx 0$) absorption from H- or He-like oxygen. The high column densities of these X-ray absorbers ($N \sim 5 \times 10^{15} - 2 \times 10^{16}\,\mathrm{cm}^{-2}$ for O VII) imply the existence of large amounts of hot gas. Given the current instrument resolution with *Chandra* and *XMM*-Newton, velocity measurements cannot distinguish its location: in the interstellar medium, in the distant halo, or in the Local Group as the intragroup medium.

No local, $z \approx 0$, absorption lines are seen in our sample. We also notice none of these targets exhibit local absorption from O VI in UV band (Sembach et al. 2003) The limits, from Table 4, are comparable to or below some of the lines detected along other lines of sight. A systematic study of detections and non-detections and their implications will be presented in a forthcoming publication. Here we note that, whatever its location, the column density of local absorption fluctuates at least by a factor of two across the sky. More specifically, for 3C 279 our 3 σ limit of $1.1 \times 10^{16}\,\mathrm{cm}^{-2}$ for O VII is well below the detected value of $\sim 1.8 \times 10^{16}\,\mathrm{cm}^{-2}$ for 3C 273 (Fang, Sembach, & Canizares 2003). These two sources are separated by an angular distance of $\sim 10°$. This corresponds to a linear scale of absorber structure of $\Delta l \lesssim 90(D/500\,\mathrm{kpc})$ kpc, for a distance to the absorber D. [11]. If the absorber is clumped on this scale, we can obtain a lower limit on the

hydrogen number density of

$$n_H \gtrsim 4 \times 10^{-3} \left(\frac{Z_O}{0.1\,Z_\odot} \right)^{-1} \left(\frac{D}{500\,\mathrm{kpc}} \right)^{-1} \mathrm{cm}^{-3}. \quad (6)$$

Here we adopt a metalicity of $Z_O \sim 0.1\,Z_\odot$ and assume half the oxygen is ionized to O VII.

6. SUMMARY

In this paper we present our *Chandra* and *XMM*-Newton observations of six quasars, with redshifts ranging from ~ 0.1 to ~ 0.9. Our main conclusions can be summarized as follows.

1. We obtained the continuum information of these six targets. All of them can be fitted quite well with a power law with absorption from neutral hydrogen, although some of these targets may require additional components to achieve a better fit.

2. Our main purpose is to search for any narrow absorption features in the X-ray spectra that were produced by the WHIM gas. After applying an optimized local fitting technique to subtract continuum, we found a total of 30 narrow features at or above 3σ lever. A cross check with different instruments excludes all features. Thus we conclude that no absorption feature was detected in our observations.

3. Given the size of our survey, we are able to put stronger constraints on cosmological parameters, compared with previous studies (see, e.g., Fang & Canizares 2000). We find the metal abundance of the IGM must be smaller than $\sim 0.3 Z_\odot$ if we adopted a *WMAP* value of Ω_m.

4. We also search for local ($z \sim 0$) absorption lines, such as those that have been detected along several other lines of sight. No local absorption line was found.

5. The limit on a ($z \sim 0$) absorber in 3C 279 compared with the detection of a strong absorption line in nearby 3C 273 indicates that the absorber has an angular scale of $\sim 10°$. If the 3C 273 absorber is in a cloud of this scale we estimate a lower limit on the hydrogen number density of $n_H \approx 4 \times 10^{-3}\,\mathrm{cm}^{-3}$. Implications will be explored further in a forthcoming publication.

Though several lines of evidence imply the existence of the WHIM gas, firm evidence for such "missing baryons" still remains an important challenge in cosmology. Future X-ray missions are very promising for detecting WHIM gas (see, e.g., Chen, Weinberg, Katz, & Davé 2003). Both *Constellation*-X [12] and *XEUS* [13] can probe highly ionized metals to column densities of as low as 10^{14} - $10^{15}\,\mathrm{cm}^{-2}$. Such high resolution and sensitivities will reveal a true "X-ray Forest" in the IGM. By comparing observations with

---

[11] A distance of 500 kpc is likely an upper limit. It is unlikely that the 3c 273 absorber has a distance from us of $\gtrsim 1$ Mpc since it will then be located even beyond our Local Group, see Fang, Sembach, & Canizares (2003) on discussion of the geometry of the Local Group and 3C 273 absorber.

[12] See http://constellation.gsfc.nasa.gov/

[13] See http://www.rssd.esa.int/index.php?project=XEUS.

numerical simulations and analytic analysis, we may eventually obtain a complete theory of structure formation and evolution from the big bang to the present epoch.

REFERENCES

Blustin, A. J., Page, M. J., & Branduardi-Raymont, G. 2004, A&A, 417, 61

Cagnoni, I., Nicastro, F., Maraschi, L., Treves, A., & Tavecchio, F. 2004, ApJ, 603, 449

Canizares, C. R. 2005, PASP, submitted

Cash, W. 1976, A&A, 52, 307

Cen, R. & Ostriker, J. P. 1999, ApJ, 514, 1

Chen, X., Weinberg, D. H., Katz, N., & Davé, R. 2003, ApJ, 594, 42

Comastri, A., Fossati, G., Ghisellini, G., & Molendi, S. 1997, ApJ, 480, 534

Costamante, L. et al. 2001, A&A, 371, 512

Cox, A. N. 2000, Allen's astrophysical quantities, 4th ed. Publisher: New York: AIP Press; Springer, 2000. Edited by Arthur N. Cox. ISBN: 0387987460

Davé, R., et al. 2001, ApJ, 552, 473

Falomo, R., Pesce, J. E., & Treves, A. 1993, AJ, 105, 2031

Fang, T., Bryan, G. L., & Canizares, C. R. 2002, ApJ, 564, 604

Fang, T. & Canizares, C. R. 2000, ApJ, 539, 532

Fang, T., Marshall, H. L., Lee, J. C., Davis, D. S., & Canizares, C. R. 2002, ApJ, 572, L127

Fang, T., Davis, D. S., Lee, J. C., Marshall, H. L., Bryan, G. L., & Canizares, C. R. 2002, ApJ, 565, 86

Fang, T., Marshall, H. L., Bryan, G. L., & Canizares, C. R. 2001, ApJ, 555, 356

Fang, T., Sembach, K. R., & Canizares, C. R. 2003, ApJ, 586, L49

Fang, T., et al. 2005, ApJ, in press

Ganguly, R., Bond, N. A., Charlton, J. C., Eracleous, M., Brandt, W. N., & Churchill, C. W. 2001, ApJ, 549, 133

Garmire, G. P., Bautz, M. W., Ford, P. G., Nousek, J. A., & Ricker, G. R. 2003, Proc. SPIE, 4851, 28

Gehrels, N. 1986, ApJ, 303, 336

Gower, A. C. & Hutchings, J. B. 1984, AJ, 89, 1658

Hamann, F., Beaver, E. A., Cohen, R. D., Junkkarinen, V., Lyons, R. W., & Burbidge, E. M. 1997, ApJ, 488, 155

Hellsten, U., Gnedin, N. Y., & Miralda-Escudé, J. 1998, ApJ, 509, 56

Houck, J. C. & Denicola, L. A. 2000, ASP Conf. Ser. 216: Astronomical Data Analysis Software and Systems IX, 9, 591

Kaspi, S., et al. 2002, ApJ, 574, 643

Lanzetta, K. M., Wolfe, A. M., & Turnshek, D. A. 1995, ApJ, 440, 435

Madejski, G. et al. 1992, Frontiers Science Series, 583

Mathur, S., Weinberg, D., & Chen, X. 2002, ApJ, 582, 82

Marshall, H. L., Cheung, T., Canizares, C. R., & Fang, T. 2003, American Astronomical Society Meeting, 202

McKernan, B., Yaqoob, T., Mushotzky, R., George, I. M., & Turner, T. J. 2003, ApJ, 598, L83

McKernan, B., Yaqoob, T., & Reynolds, C. S. 2004, ApJ, 617, 232

Miley, G. K. & Hartsuijker, A. P. 1978, A&AS, 34, 129

Nicastro, F. et al. 2002, ApJ, 573, 157

Nicastro, F., et al. 2005, Nature, 433, 495

Perna, R. & Loeb, A. 1998, ApJ, 503, L135

Polomski, E., Vennes, S., Thorstensen, J. R., Mathioudakis, M., & Falco, E. E. 1997, ApJ, 486, 179

Press, W. H. & Schechter, P. 1974, ApJ, 187, 425

Rachen, J. P., Mannheim, K., & Biermann, P. L. 1996, A&A, 310, 371

Rasmussen, A., Kahn, S. M., & Paerels, F. 2003, ASSL Vol. 281: The IGM/Galaxy Connection. The Distribution of Baryons at z=0, 109

Reeves, J. N. & Turner, M. J. L. 2000, MNRAS, 316, 234

Remillard, R. A., Tuohy, I. R., Brissenden, R. J. V., Buckley, D. A. H., Schwartz, D. A., Feigelson, E. D., & Tapia, S. 1989, ApJ, 345, 140

Sambruna, R. M. 1997, ApJ, 487, 536

Sambruna, R. M., George, I. M., Madejski, G., Urry, C. M., Turner, T. J., Weaver, K. A., Maraschi, L., & Treves, A. 1997, ApJ, 483, 774

Savage, B. D., Tripp, T. M., & Lu, L. 1998, AJ, 115, 436

Sembach, K. R., et al. 2003, ApJS, 146, 165

Simcoe, R. A., Sargent, W. L. W., & Rauch, M. 2002, ApJ, 578, 737

Singh, K. P., Rao, A. R., & Vahia, M. N. 1991, A&A, 243, 67

Spergel, D. N., et al. 2003, ApJS, 148, 175

Spitzer, L. 1978, New York Wiley-Interscience, 1978, p. 333

Tripp, T. M. & Savage, B. D. 2000, ApJ, 542, 42

Tripp, T. M., Savage, B. D., & Jenkins, E. B. 2000, ApJ, 534, L1

Ueda, Y., Ishisaki, Y., Takahashi, T., Makishima, K., & Ohashi, T. 2001, ApJS, 133, 1

Verner, D. A., Verner, E. M., & Ferland, G. J. 1996, Atomic Data and Nuclear Data Tables, 64, 1

Viel, M., Branchini, E., Cen, R., Matarrese, S., Mazzotta, P., & Ostriker, J. P. 2003, MNRAS, 341, 792

Whitney, A. R. et al. 1971, BAAS, 3, 465

Wilkes, B. J. & Elvis, M. 1987, ApJ, 323, 243

Williams, R. et al. 2005, ApJ, submitted (astro-ph/0504558)

Wolter, A. et al. 1998, A&A, 335, 899

Wood, K. S. et al. 1984, ApJS, 56, 507

Yoshikawa, K., Yamasaki, N. Y., Suto, Y., Ohashi, T., Mitsuda, K., Tawara, Y., & Furuzawa, A. 2003, PASJ, 55, 879